

Optimum Beam Configurations in Tomographic Intensity Modulated Radiation Therapy

Matthew Braunstein and Robert Y. Levine
Spectral Sciences, Inc., 99 S. Bedford St, # 7, Burlington, MA 01803-5169, USA

Short Title

Optimum Beam Configurations in Tomographic IMRT

Keywords

intensity modulated radiation therapy, tomography, beam number, beam orientation.

PACS Number 87.53.kn.

Abstract

We review and extend the theory of tomographic dose reconstruction for intensity modulated radiotherapy (IMRT). We derive the basis for a saturation with beam number of dose conformation, and provide an analysis which ranks particular beam orientations in terms of the contribution to the delivered dose. Preferred beam directions are found which effectively reduce the number of beams necessary to achieve a given level of dose conformation. The analysis is a new application of the tomographic Projection-Slice Theorem to the problem of beam orientation determination. The effects of the beam front filter and the positivity constraint arising from the tomographic approach are analyzed, and modifications of the beam front filter for small beam numbers are suggested. The theory is applied to simple geometric shapes in two dimensions. A Gaussian ellipse, where analytical results are obtained, and simple hard-edged convex prescribed dose shapes are examined to illustrate beam selection based on the beam overlap metric. More complex concave prescribed dose shapes which contain a sensitive organ are also analyzed and for low beam numbers are found to have preferred beam directions.

1. Introduction

Intensity modulated radiation therapy (IMRT) involves the delivery of multiple modulated x-ray beams at various orientations relative to the patient. The goal is the delivery of a lethal radiation dose to the tumor volume (TV) with minimum dose to normal tissues and organs-at-risk (OARs). The dose inversion problem is the determination of the best combination of beam orientations and modulation patterns to approximate a prescribed dose. In practice, these are often found by trial and error simulation studies of the delivered dose by the medical physicist and physician, guided by their experience base. However, the large number of possible beam angles and modulation patterns make this approach to an optimal dose plan difficult and time-consuming for IMRT.

Many computational methods of solving the inversion problem in radiation therapy have been studied. Some examples include simulated annealing (Webb 1989, Webb 1991, Mageras and Mohan 1993), constrained random search (Neimierko 1992), maximum likelihood estimation (Llacer 1997), projection onto convex sets (Lee *et al* 1997, Cho *et al* 1998), linear programming (Rosen *et al* 1991) and non-linear feasibility search (Censor *et al* 1988). Reviews are found in Webb 1993 and Boyer 1993. In the early 1980s it was realized that the tomographic theory of projections could be used to approximate the relationship between intensity modulated beams and the delivered dose (Brahme *et al* 1982). A series of articles demonstrated that the same powerful mathematical framework used in CT, MRI, and ECT to reconstruct tissue images from projections could be used to solve the inverse problem of determining beam orientations and modulation patterns from a dose prescription (Cormack 1987, Cormack and Cormack 1987, Cormack and Quinto 1989, Cormack and Quinto 1990, Bortfeld *et al* 1990, Mackie *et al* 1993, Holmes and Mackie 1994, Bortfeld and Boyer 1995). Among the advantages of the tomographic approach is that it is very intuitive, building into the

mathematical formalism the use of beam's-eye-view projections of the tumor to define the beam front. The projection automatically compensates for fluence attenuation as the tumor is traversed, so that normal tissue exposure is reduced. In addition, the projection formalism is cast in such a way that basic results can be derived analytically for simple tumor shapes. Furthermore, the method avoids many of the numerical difficulties of search algorithms as each orientation is independently processed in projecting the dose onto the beam front. This becomes especially relevant when full 3D geometries are considered with a large number of potential beam locations and modulation patterns (Gregerson *et al* 1995, Levine *et al* 1999). While IMRT beam numbers have been determined for some important cases such as the prostate (Stein *et al* 1997), the factors increasing beam numbers, such as dose resolution, may force consideration of many more beams for precision conformal therapy. Unlike standard tomographic reconstruction of images from measured projection profiles, the inversion of the prescribed dose results in photon fluences which may be negative and therefore unphysical. This must be removed by a positivity constraint, a condition that directs the unavoidable exposure to nearby healthy tissues. The tomographic analogy for IMRT is further complicated by low beam numbers and a beam/dose model with fluence attenuation and electron transport; effects that must be incorporated into an approximate tomographic model. However, unlike in CT, the goal of the reconstruction, the prescribed dose, is known *apriori*. Therefore, optimum beam orientations are derivable.

In this paper the theory of tomographic dose reconstruction is reviewed and extended. The results of the theory are applied to simple geometrical shapes to illustrate the basic results, and to more complex and realistic dose prescriptions. One of the main issues considered is the number of beams required to reconstruct a given prescribed dose; and the existence of preferred beam directions which may be used to reduce the number of beams sufficient to achieve a certain level of conforming dose.

The consensus in beam orientation determination appears to be that for more than about five beams, there is negligible improvement over a uniform array of beams (Bortfeld and Schlegel 1993, Oldham *et al.* 1998). With fewer numbers of beams, however, preferred directions can be obtained by a global search in the space of beam orientations with multiple local minima (Bortfeld and Schlegel 1993). Oldham *et al.* (1998) have similarly illustrated the idea of preferred directions with the use of a “beam-cost plot” of an objective function which depends on the couch and gantry angles. Llacer (1997) derives preferred beam directions from a curvature-based measure of the prescribed dose function. A goal of the present work is to motivate the existence of these preferred directions by setting them on a firm mathematical foundation through consideration of the frequency space properties of the prescribed dose function. Our approach is based on the properties of the prescribed dose in frequency space through the tomographic Projection-Slice Theorem, which also provides an estimate of the required beam number from the number of cylindrical harmonics in the Fourier transform. While the conclusions are similar to the above mentioned references, the application of tomographic sampling theory to IMRT inversion in this way is to our knowledge unique.

The choice of optimum beam number and orientations that are clinically achievable is not well understood. Current treatment protocols involve fewer than 20 beams, which can be an extreme undersampling of the optimum continuous beam profile functions. In the literature, IMRT beam number estimates range from 32 on a cylindrically symmetric phantom (Webb 1989), nine coplanar beams for nasopharynx (Bortfeld *et al.* 1990) and prostate (Bortfeld *et al.* 1994), 5-6 beams for prostate (Spirou and Chui 1998), to as few as 3-5 beams for general treatment (Oldham *et al.* 1998, Haas *et al.* 1998, Soderstrom and Brahme 1993). Alternative approaches to the inversion problem that search the space of beam configurations have been too slow for a fine resolution search of beam number and orientations (Stein *et al.* 1997, Oldham *et al.* 1998, Haas *et al.* 1998, Rowbottom *et al.*

1998). Although the use of very few beam numbers has been advocated recently (Stein *et al* 1997, Oldham *et al* 1998, Spirou and Chui 1998, Soderstrom and Brahme 1993) to achieve tumor dose homogeneity with acceptable conformation, new applications of high precision radiosurgery (Oldham *et al* 1998, Cardinale *et al* 1998) to concave tumors suggest the need to examine the trade-off between the dose edge and tumor dose heterogeneity with many beams. Because this trade-off involves the delivered dose function frequency content, a more general framework for the analysis of beam number and orientation, as presented here, may be useful.

The effects of the physical constraint of positive beam profiles on the tomographic inversion algorithm and on the achievable delivered dose are also considered. We illustrate these effects with simple examples and find that, while this constraint results in unavoidable normal tissue exposure, the tomographic approach is superior to dose projection alone even with small beam numbers. The effects of the mathematical beam front filter, a high pass filter which is part of the tomographic formalism and is important in achieving a conforming dose (Bortfeld and Boyer 1995), are also discussed. A natural generalization of the filters is suggested for small beam numbers.

In Section 2, the formal theory for IMRT inversion including fluence attenuation and electron transport is presented. For clarity, we restrict our analysis to two dimensions, but have already shown how the theory can be extended to three dimensions (Gregerson *et al* 1995, Levine *et al* 1999). The basis for beam number saturation and the ranking of beam orientation from a given prescribed dose is derived. In Section 3, we illustrate beam number saturation and preferred orientation effects with a Gaussian ellipse dose prescription, for which results can be obtained analytically, and discuss the effect of the beam front filter and the positivity constraint on the delivered dose. In Section 4, these issues are examined numerically with a series of geometric shapes closer to a clinical prescription:

convex dose functions including an elliptical dose function, a “peanut” shaped tumor, an elliptical shaped tumor with an organ-at-risk, and more complex concave dose functions including a “butterfly” shaped tumor, and a “horseshoe” shaped tumor enclosing an organ-at-risk. We find that beam number and preferred direction effects, as well as the importance of including the beam front filter, carry over to the more realistic dose prescriptions. The conclusions follow in Section 5.

2. Tomographic IMRT Formalism

2.1. Dose Inversion

In this section the formalism of tomographic dose delivery in two dimensional IMRT is reviewed (Cormack 1987, Cormack and Cormack 1987, Cormack and Quinto 1989, Cormack and Quinto 1990, Bortfeld *et al* 1990, Mackie *et al* 1993, Holmes and Mackie 1994, Bortfeld and Boyer 1995). The generalization to three dimensions, which permits enhanced dose conformation and organ-at-risk shielding, can be found in Levine *et al.* 1999. Figure 1 contains the description of 2D tomographic IMRT consisting of a gamma ray beam profile $f(\theta, s)$ at an angle θ relative to the tissue space coordinate system. The treatment beam rotates at a radius R_0 about the treatment isocenter, which is typically in the center of the tumor. It is assumed that the projected extent of the treatment volume is contained in the modulated beam front.

The total dose to the point \bar{x} in the tissue is the integral over θ of the dose due to $f(\theta, s)$. For a profile at angle θ , define $\tau(\theta, \bar{x} \cdot \hat{\theta})$ to be the distance in air from the tissue surface to the beam front (at $s = \bar{x} \cdot \hat{\theta}$) along a ray that intersects the point \bar{x} . As seen in figure 1, $\hat{\theta}$ denotes the vector $(\sin \theta, -\cos \theta)$ along the beam front and $\hat{\theta}^\perp = (\cos \theta, \sin \theta)$ is normal to the beam. For notational

clarity, the superscripts \wedge and \rightarrow on $\hat{\theta}$, $\hat{\theta}^\perp$, \bar{x} and \bar{y} will be removed from dot products in the remainder of this section. The depth in tissue to the point \bar{x} along the ray is given by

$$d(\theta, \bar{x}) = (R_0 - \tau(\theta, x \cdot \theta) - x \cdot \theta^\perp). \quad (1)$$

The photon fluence $I(\theta, x \cdot \theta)$ from the beam front location $s = x \cdot \theta$ is assumed to be exponentially attenuated in the tissue with attenuation constant μ . The result is

$$I(\theta, x \cdot \theta) = e^{-\mu d(\theta, x)} f(\theta, x \cdot \theta). \quad (2)$$

Radiation dose $D(\theta, \bar{x})$ results from the interaction of the photons with electrons primarily by Compton scattering and pair production (Johns and Cunningham 1983). It is assumed that the effects of subsequent electron transport can be modeled as a 2D convolution of the photon fluence in the tissue

$$D(\theta, \bar{x}) = \frac{\mu_{en}}{\rho} \int d\bar{y} \kappa_\theta(\bar{y}) e^{-\mu d(\theta, \bar{x} - \bar{y})} f(\theta, (x - y) \cdot \theta) \quad (3)$$

where there is, in general, a beam angle dependence in the dose kernel κ . The dose kernel from beam θ at the point \bar{x} is roughly an ellipse whose long axis extends along the direction $\hat{\theta}^\perp$. The factor μ_{en} / ρ converts the photon fluence to delivered dose in tissue of density ρ and energy deposition constant μ_{en} (Johns and Cunningham 1983). The functional form of the dose kernel $\kappa_\theta(\bar{y})$ for homogeneous tissue is given by

$$\kappa_\theta(\bar{y}) = \kappa(y \cdot \theta, y \cdot \theta^\perp) \quad (4)$$

reflecting rotation of the kernel with the beams. Figure 2 contains a representation of multi-beam dose delivery in which the rotated kernels in Eq. (4) are shown.

The total tomographic dose is given by the integral over all beam directions as

$$D(\bar{x}) = \int d\theta D_\theta(\bar{x}) = \frac{\mu_{en}}{\rho} \int d\theta \int d\bar{y} \kappa(y \cdot \theta, y \cdot \theta^\perp) e^{-\mu d(\theta, \bar{x} - \bar{y})} f(\theta, (x - y) \cdot \theta), \quad (5)$$

which upon substitution of equation (1) yields

$$D(\bar{x}) = \frac{\mu_{en} e^{-\mu R_0}}{\rho} \int d\theta \int d\bar{y} \kappa(y \cdot \theta, y \cdot \theta^\perp) e^{\mu(x-y) \cdot \theta^\perp} [e^{\mu\tau(\theta, \theta \cdot (x-y))} f(\theta, (x - y) \cdot \theta)]. \quad (6)$$

Changing the \bar{y} integration variable to $\xi = y \cdot \theta$ and $\eta = y \cdot \theta^\perp$, the integral in equation (6) is written

$$D(\bar{x}) = \frac{\mu_{en} e^{-\mu R_0}}{\rho} \int d\theta \int d\xi d\eta \kappa(\xi, \eta) e^{-\mu\eta} e^{\mu x \cdot \theta^\perp} [e^{\mu\tau(\theta, \theta \cdot x - \xi)} f(\theta, \theta \cdot x - \xi)]. \quad (7)$$

Defining the θ -independent scattering kernel

$$\kappa_\mu(\xi) = \int d\eta e^{-\mu\eta} \kappa(\xi, \eta), \quad (8)$$

the expression in equation (7) is written in the desired form,

$$D(\bar{x}) = \frac{\mu_{en} e^{-\mu R_0}}{\rho} \int d\theta e^{\mu x \cdot \theta^\perp} (\kappa_\mu \otimes H)(\theta, x \cdot \theta), \quad (9)$$

where \otimes denotes the one-dimensional (beam front) convolution, and

$$H(\theta, s) \equiv e^{\mu\tau(\theta, s)} f(\theta, s) \quad (10)$$

is the modulated beam front f compensated by the factor $e^{\mu\tau(\theta, s)}$ for a non-planar tissue-air interface. The expression in equation (9) is the dual attenuated Radon transform of the convolved, compensated beam profile $(\kappa_\mu \otimes H)$ which is denoted (Natterer 1986),

$$D = \frac{\mu_{en} e^{-\mu R_0}}{\rho} T_{\mu}^{\#}(\kappa_{\mu} \otimes H). \quad (11)$$

The goal of IMRT planning is the inversion of equation (11) to obtain a beam profile $f(\theta, s)$ for a prescribed dose function $P = D$. The formal inversion of equation (11) follows from a theorem that states that for any function $g : \mathfrak{R}^2 \rightarrow \mathfrak{R}$,

$$g = \frac{1}{4\pi} T_{\mu}^{\#} I_{-\mu}^{-1} T_{-\mu} g, \quad (12)$$

where

$$T_{-\mu} g = \int_{x \cdot \theta = s} e^{-\mu x \cdot \theta^{\perp}} g(\bar{x}) d\bar{x} \quad (13)$$

is the attenuated Radon transform and $I_{-\mu}^{-1}$ is a beam front filter operator (Bortfeld and Boyer 1995, Gregerson *et al* 1995, Levine *et al* 1999) defined by

$$\widehat{(I_{-\mu}^{-1} f)}(\sigma) = \begin{cases} |\sigma| \hat{f}(\sigma) & |\sigma| > |\mu| \\ 0 & \text{otherwise} \end{cases}, \quad (14)$$

where \wedge denotes Fourier transform, and where σ is the spatial frequency variable. The expression in equation (12) suggests that for a prescribed dose function $P = D$, the inversion of equation (11) is given by

$$f(\theta, s) = \frac{\rho}{4\pi\mu_{en}} e^{\mu R_0 - \mu\tau(\theta, s)} \kappa_{\mu}^{-1} \otimes (I_{-\mu}^{-1} T_{-\mu} P). \quad (15)$$

This is the basic result of tomographic IMRT inversion relating the prescribed dose to the beam front. The inversion algorithm suggested by equation (15) consists of a μ -compensated projection of the dose, defined in equation (13), followed by two beam front filters arising from the rotational

treatment geometry ($I_{-\mu}^{-1}$) and electron transport (κ_{μ}^{-1}). The filters $I_{-\mu}^{-1}$ and κ_{μ}^{-1} accentuate the high frequency content of the projection. The reason for the filter $I_{-\mu}^{-1}$ is not intuitive, but can be related to the sampling density in the Fourier space of the prescribed dose function (see Section 2.4 and Bortfeld and Boyer 1995). The use of a μ -compensated projection, $T_{-\mu}$, is a new component of the basic formalism (Bortfeld and Boyer 1995, Gregerson *et al* 1995, Levine *et al* 1999), and automatically takes into account attenuation effects as the tumor is traversed so that more dose is deposited where the tumor is wide. There is also an overall correction factor due to the tissue-air boundary given by $e^{-\mu\tau(\theta,s)}$.

Unlike in CT processing, however, the filtered beam obtained from the formal inversion above represents a physical photon fluence. Consequently, a positivity constraint must be applied to $f(\theta, s)$ by setting negative fluence to zero (Brahme *et al* 1982, Cormack and Quinto 1989, Cormack and Quinto 1990, Bortfeld *et al* 1990). Negative fluence arises mathematically from the application of the filter operator $I_{-\mu}^{-1}$, to the positive profile $T_{-\mu}P$ in Eq. (13). The negative values in a beam are typically near the edges of the beam front to cancel the positive fluence values (on rays intersecting the tumor) from other beams in normal tissue. The dose predicted from beams in which the unphysical negative fluence is zeroed has unavoidable normal tissue exposure. Modulated beam fronts without negative fluence are obtained by dose projection alone; that is, by dropping the $I_{-\mu}^{-1}$ filter in equation (15). This is a very intuitive approach to IMRT, because the outline of the tumor determines beam port shape. It can be shown, however, that without the filter the delivered dose in equation (11) is approximately a 2D $1/r$ convolution of the prescribed dose (Natterer 1986), resulting in a delivered dose which is less conforming than that with the filter present. This effect, which is especially evident for larger beam numbers, is discussed further in Sections 3 and 4. It is

shown that the application of filter operator $I_{-\mu}^{-1}$ and the positivity constraint results in less normal tissue exposure than dose projection alone.

2.2 Beam Number Saturation

The number of beams required for 2D tomographic reconstruction is a classic problem in the field addressed in Crowther *et al* 1970. In this section a similar argument is used to obtain beam number estimates based on equation (11) and the Projection-Slice Theorem. We will show that the expansion of the prescribed dose in cylindrical harmonics is related to the number of beam directions. This relationship puts a condition on the number of beams required to reconstruct a given prescribed dose. As an aside, it is interesting that inversion of dose cylindrical harmonics was recently proposed as the basis of a tomographic IMRT reconstruction algorithm (Cormack 1998, Oelfke and Bortfeld 1999).

The Projection-Slice Theorem (Natterer 1986) states that for a function, $g : \mathfrak{R}^2 \rightarrow \mathfrak{R}$, the Fourier transform of the projection is related to a slice of the 2D Fourier transform by

$$(T_{-\mu}^{\wedge}g)(\theta, \sigma) = \sqrt{2\pi} \hat{g}(\sigma\theta - i\mu\theta^{\perp}). \quad (16)$$

Multiplying both sides of equation (15) by $e^{\mu\tau(\theta,s)}$ and taking the Fourier transform results in the expression

$$\hat{H}(\theta, \sigma) = \begin{cases} \frac{\rho e^{\mu R_0}}{2\sqrt{2\pi}\mu_{en}} \frac{|\sigma|}{\hat{\kappa}_{\mu}(\sigma)} \hat{D}(\sigma\theta - i\mu\theta^{\perp}) & |\sigma| > \mu \\ 0 & otherwise \end{cases} \quad (17)$$

where $H(\theta, s)$ is the surface-compensated beam front in equation (10). For high energy x-rays ($> 1MeV$) the extinction length μ^{-1} is large compared to the length scales in the prescribed dose

function (Johns and Cunningham 1983), so it is dropped in the following discussion. In the limit $\mu \rightarrow 0$, the dose function \hat{D} in equation (17) is written

$$\hat{H}(\theta, \sigma) = \frac{\rho e^{\mu R_0}}{2\sqrt{2\pi\mu_{en}} \hat{\kappa}_\mu(\sigma)} \frac{|\sigma|}{\sigma} \hat{D}(\sigma\theta), \quad (18)$$

which relates the 1D beam front Fourier transform to a slice of the 2D dose Fourier transform.

Expanding the 2D dose function \hat{D} in N cylindrical harmonics, we have

$$\hat{D}(\sigma\theta) = \sum_{n=-N}^N G_n(\sigma) e^{in\theta}. \quad (19)$$

Note from equation (18) that the set of coefficients $\{G_n(\sigma)\}$, which completely determines the dose function, is linearly related to the set of beam modulation patterns for fixed σ . Assuming M beams at angles $\{\theta_j, j = 1, \dots, M\}$, the M equations for $(2N + 1)$ harmonic coefficients are given from equation (18) by

$$\sum_{n=-N}^N G_n(\sigma) e^{in\theta_j} = \frac{2\sqrt{2\pi\mu_{en}} e^{-\mu R_0}}{\rho} \frac{\hat{\kappa}_\mu(\sigma)}{|\sigma|} \hat{H}(\theta_j, \sigma), \quad j = 1, \dots, M. \quad (20)$$

The required beam number to determine the unknown harmonic coefficients $\{G_n(\sigma)\}$ is then given by

$$M \geq (2N + 1), \quad (21)$$

where N is determined by the condition $|G_n(\sigma)| \rightarrow 0, \forall \sigma, \forall n > N$.

In traditional image reconstruction, the condition in equation (21) is related to the spatial frequencies and size of the reconstructed object using the Bessel Function transform between the

cylindrical harmonics of Fourier transform pairs in two dimensions (Crowther *et al* 1970). The result is an approximate sufficient beam number given by

$$M \approx \pi RW / 2, \quad (22)$$

where R and W are the radius and maximum spatial frequency of the reconstructed function, respectively (Bortfeld *et al* 1990). This ‘‘Bow Tie’’ condition is a very conservative bound arising from the Debye approximation for Bessel functions with large order (Natterer 1986, Crowther *et al* 1970, Lindgren and Rattey 1981). Because the dose function is known *a priori* in IMRT, however, the computation of $\{G_n(\sigma)\}$ in equation (19) is possible for a direct estimate of required beam numbers. This is shown in Section 3 for an elliptical Gaussian dose, where the harmonic coefficients can be determined analytically, as well as other more clinical prescribed dose functions.

2.3. Beam Orientation Metric

In this section tomographic IMRT is applied to obtain an approximate orientation metric for beams; that is, an angle-dependent function ranking beam orientations for the relative contribution to dose reconstructions. Consider the overlap of two beam profiles $\{f_i(\theta, s), i = 1, 2\}$ defined by

$$(f_1, f_2) = \int d\theta \int ds f_1(\theta, s) f_2(\theta, s), \quad (23)$$

and of two tissue space dose functions $\{D_i(x), i = 1, 2\}$ given by

$$[D_1, D_2] = \int dx D_1(x) D_2(x). \quad (24)$$

It can be shown that the dual Radon transform in equation (11) for $\mu = 0$ is, in fact, the metric dual of the Radon transform (Natterer 1986). In terms of the definitions in equations (23) and (24), this relationship can be expressed as

$$[T_0^\# f, D] = (f, T_0 D) \quad (25)$$

for arbitrary dose (D) and profile (f) functions. For a prescribed dose function $P(x)$ defining the beam profile in equation (15), the delivered dose from the j^{th} beam is

$$D_{\theta_j}(x) = \frac{\mu_{en} e^{-\mu R_0}}{\rho} T_\mu^\# [(\kappa_\mu \otimes H)(\theta_j, s)], \quad (26)$$

where H is defined in equations (10) and (15) with $D = P$. The overlap of $D_{\theta_j}(x)$ with the prescribed dose $P(x)$ for $\mu = 0$ (in $T_\mu^\#$) is

$$[P(x), D_{\theta_j}(x)] = \frac{\mu_{en} e^{-\mu R_0}}{\rho} [P(x), T_0^\# (\kappa_\mu \otimes H)] = \frac{\mu_{en} e^{-\mu R_0}}{\rho} (T_0 P, \kappa_\mu \otimes H), \quad (27)$$

which upon substitution of equations (10) and (15) yields

$$[P(x), D_{\theta_j}(x)] = \frac{1}{4\pi} \int T_0 P(\theta_j, s) (I_0^{-1} T_0 P(\theta_j, s)) ds. \quad (28)$$

The expression on the right-hand side of equation (28) is an angle dependent measure defined on the beam profiles known as the ρ -metric (Medoff 1987) which measures the overlap of the dose contributed from beam angle j with the prescribed dose. Note that the angle metric is independent of the electron transport kernel κ . Optimization of the overlap implicitly assumes that the prescribed and delivered dose functions are normalized such that $[P, P] = [D, D] = \text{constant}$. Assuming a normalization constant of unity, we have

$$[P - D, P - D] = 2 - 2[P, D], \quad (29)$$

so that maximum overlap $[P, D]$ corresponds to minimum discrepancy between delivered and prescribed dosages. The normalization condition is only approximately valid in IMRT because the

dose is usually normalized to 100% tumor coverage by the prescription, rather than an integral condition $[P, P] = [D, D] = 1$. In Section 3 the measure is applied to an elliptical dose prescription for an analytical estimate of optimum beam orientations. In addition, more general beam orientation criteria based on sampling theory is suggested.

3. Analytic results for the Gaussian Ellipse

In this section the formalism developed in Section 2 is applied to simple dose functions to illustrate basic results, including beam number saturation and orientation effects. This is done with a Gaussian ellipse prescribed dose for which tomographic IMRT beam fronts and other properties can be derived analytically. Beam front positivity constraint and sampling effects are also discussed with this model. In Section 4, we demonstrate numerically how these results extend to more clinically relevant prescribed dose shapes. The results taken together demonstrate heuristic guidelines for the inversion problem derivable from tomographic IMRT.

3.1 Beam Thresholds

In this section an elliptical Gaussian dose function centered at (x_0, y_0) given by

$$P(x, y) = \exp\left(-\frac{(x - x_0)^2}{a^2} - \frac{(y - y_0)^2}{b^2}\right), \quad (30)$$

is used as the input to IMRT dose inversion. Although equation (30) does not represent a typical prescribed dose function, it provides an analytic testbed for the concepts discussed in Section 2.

In Section 2 it was suggested that the number of beams required for dose reconstruction is linearly dependent on the number of cylindrical harmonics in the Fourier transform of the dose

function. This number can be computed analytically for $P(x, y)$ in equation (30) by consideration of the Fourier transform,

$$\hat{P}(k, \phi) = \pi ab \exp(-2\pi ikr \cos \phi) \exp[-\pi^2 k^2 (a^2 \cos^2 \phi + b^2 \sin^2 \phi)], \quad (31)$$

where without loss of generality, $x_0 = r, y_0 = 0, k_x = k \cos \phi$, and $k_y = k \sin \phi$. By repeated use of the identity

$$\exp(-2\pi ikr \cos \phi) = \sum_{l=-\infty}^{\infty} i^l J_l(-2\pi kr) e^{il\phi}, \quad (32)$$

the expansion in equation (19) is computed for $\hat{P}(k, \phi)$ to obtain

$$\hat{P}(k, \phi) = \sum_{p=-\infty}^{\infty} G_p(k, r) e^{ip\phi}, \quad (33)$$

with

$$G_p(k, r) = i^p \pi ab \exp\left(-\frac{\pi^2 (a^2 + b^2) k^2}{2}\right) \sum_{m=-\infty}^{\infty} J_{2m-p}(2\pi kr) I_m\left(\frac{\pi^2 (a^2 - b^2) k^2}{2}\right), \quad (34)$$

where $\{J_n\}$ and $\{I_m\}$ are the Bessel and associated Bessel functions, respectively. In the limit $r \rightarrow 0$, equation (34) is written,

$$G_{2m}(k, 0) = (-1)^m \pi ab \exp\left(-\frac{\pi^2 (a^2 + b^2) k^2}{2}\right) I_m\left(\frac{\pi^2 (a^2 - b^2) k^2}{2}\right). \quad (35)$$

A comparison of equations (34) and (35) suggests that the effect of a tumor offset ($r \neq 0$) is to add in lower ordered Bessel functions to the harmonic coefficients, and thereby increase the relative value of the coefficient. The resulting increase in beam number suggests the intuitive fact that the most efficient use of beams is with the isocenter at the center of the tumor.

Figure 3 contains plots of the cylindrical harmonic coefficients, $G_{2m}(k,0)$, for a Gaussian ellipse with dimensions $(a,b) = (5,1)$, and $(10,1)$. The spatial frequency unit for k , typically cm^{-1} , is the inverse of the unit for a and b . As the tumor becomes more elongated and larger, more cylindrical harmonics contribute to the delivered dose. Also note that the harmonics fall off monotonically with increasing beam number, $2m$. By cutting off the contribution at $\sim 1\%$ of the maximum, estimates of 15 and 20 nonzero harmonics are obtained for a of 5, and 10, respectively, indicating rough beam numbers in the dose reconstruction. We expect beam number saturation to extend to more typical dose prescriptions with step function edges. These are investigated numerically in Section 4 to demonstrate the existence of beam numbers beyond which there is negligible improvement in the delivered dose. That number is greater for a more elongated or irregularly-shaped tumor with a greater number of cylindrical harmonic coefficients.

3.2 Beam Metrics and Preferred Orientations

We now derive the beam metric as described in Section 2, and rank the relative importance of particular beam orientations for the Gaussian ellipse dose prescription. This is done by computing the overlap of the prescribed dose and the delivered dose from a particular beam direction as shown in equation (27). We first use equation (15) to derive the beam front, and then find its overlap with the prescribed dose.

Neglecting electron transport effects (κ_0 is not considered) and assuming the tumor is small compared to the attenuation length ($\mu = 0$), substitution of equation (30) into equation (15) yields the IMRT beam front,

$$f(\theta, s) = \frac{\rho}{4\pi\mu_{en}} I_0^{-1} T_0 P = \frac{2ab}{\pi\omega^2(\theta)} \left[\frac{1}{2} - \frac{s}{\omega(\theta)} \exp[-s^2 / \omega^2(\theta)] E(s / \omega(\theta)) \right], \quad (36)$$

where

$$E(y) = \int_0^y e^{x^2} dx, \quad (37)$$

and

$$\omega(\theta) = \sqrt{a^2 \cos^2 \theta + b^2 \sin^2 \theta}. \quad (38)$$

Substitution of equation (30) into equation (13) with $\mu = 0$ yields the Radon transform of the prescribed dose, $P(x, y)$, given by

$$T_0 P = \frac{ab\sqrt{\pi}}{\omega(\theta)} \exp(-s^2 / \omega^2(\theta)) \quad (39)$$

which is, as expected, a Gaussian function with angle-dependent width. The substitution of the positively constrained expressions in equations (36) and (39) into equation (27) yields the overlap contribution of the beam at angle θ to the Gaussian dose prescription,

$$M(\theta) = [P(\bar{x}), D_\theta(\bar{x})] = \frac{2a^2b^2}{\sqrt{\pi}\omega^3} \int_{-\infty}^{\infty} ds e^{-s^2/\omega^2} \left(\frac{1}{2} - \frac{s}{\omega} e^{-s^2/\omega^2} E(s/\omega) \right) \Omega\left(\frac{s}{\omega} - \xi_0\right), \quad (40)$$

where E and ω are given in equations (37) and (38), and Ω is one minus the Theta function ($\Omega(r) = 0, r \geq 0$, and $\Omega(r) = 1$, otherwise). The parameter ξ_0 in equation (40) is the point along the beam front where the fluence becomes negative (see figure 6). Changing the integration variable to $u = s / \omega$ in equation (40) yields

$$M(\theta) = \frac{a^2b^2J}{a^2 \cos^2 \theta + b^2 \sin^2 \theta}, \quad (41)$$

where J is the numerical constant

$$J = \frac{2}{\sqrt{\pi}} \int_{-\infty}^{\infty} du e^{-u^2} (0.5 - ue^{-u^2} E(u)) \Omega(u - \xi_0). \quad (42)$$

Equation (41) is the beam metric for the Gaussian ellipse and is the chief result of this section. It can be immediately seen that for ellipses with $a > b$, angles near 90° and 270° along the long axis of the ellipse have larger beam metric values, while the function is smallest at 0° and 180° . Angles along the 90° and 270° directions will therefore contribute more to the reconstruction. As expected, for circular ellipses, $a = b$, there is no direction preference. Figure 4 contains a plot of the beam selection metric, $M(\theta)$, normalized to a maximum of 1.0 for the Gaussian ellipse dose prescription in equation (30) with $a=4\text{cm}$ and $b=0.8\text{cm}$. The prescribed dose is also shown in the figure. Beam selection maxima occur along the narrow ends of the ellipse as expected. These orientations correspond to beams at 90° to the bottom of the figure. This property also holds for more realistic dose prescriptions with hard edges considered in Section 4. Intuitively these beam directions are preferred because high pass filtering of the projected dose to obtain the beam front accentuates the directions with higher varying (higher frequency) projections. Even without beam filtering, the beam metric is an overlap function which will be larger for directions with narrower projected doses. This is clear if we consider a uniform rectangular prescribed dose of length l_a and l_b , with $l_a > l_b$ (see Bortfeld and Schlegel 1993 for a similar argument). The beam metric along the narrow projection, M_1 , will have a width l_b and will be proportional to $l_b l_a^2$. The beam metric along the wide end, M_2 , will have a width l_a and will be proportional to $l_a l_b^2$, so that $M_1 > M_2$, and the narrow projection direction will be preferred.

The beam selection metric can reduce the number of beams necessary to reconstruct the prescribed dose compared to using beams evenly spaced around the tumor. Dose conformation for

the Gaussian ellipse was judged by a scatterplot, which is defined as a plot of delivered versus prescribed dose over the set of pixels in the tissue. The limit of perfect reconstruction is revealed by the alignment of the scatterplot along the 45° line, where the delivered and prescribed doses are equal. The delivered dose is obtained by the application of equations (10) and (11) to beam fronts defined by equation (15) with the Gaussian ellipse dose described above. Although these functions are analytic, finite sampling here and elsewhere in this study was done at 0.1cm for convenience. The Nyquist limit for this sampling is 5cm^{-1} , well above the frequency content in the prescribed dose shown in figure 3. Numerical results were compared with analytic results for accuracy. For these calculations and those elsewhere in the paper, attenuation and electron scatter effects were neglected.

Figure 5 contains isodose contours and scatterplots of delivered versus prescribed dose for the $(a, b) = (4.0, 0.8)$ Gaussian ellipse. Results are shown for 50, 18, and 10 modulated beams with even angular spacing between 0° and 180° degrees (with no attenuation or scatter effects these directions are equivalent to angles between 180° and 360°). Also shown is the scatterplot for 10 modulated beams selected at an even angular spacing between 45° and 135° that correspond to the highly weighted angles of the beam metric shown in figure 5. An overall fluence normalization factor is applied to match the prescribed dose value of 1.0 at the isocenter. With 50 beams, there is nearly perfect reconstruction except for unavoidable overdosage below 20% of the dose maximum, which is due to the positivity constraint. Without this constraint, there is nearly perfect reconstruction with 50 beams. With 18 beams, which is close to the saturation point derived from the cylindrical harmonic expansion of the prescribed dose in figure 3, this overdose becomes slightly worse. With 10 beams, the overdosing is severe so that low prescribed dose regions receive as much as 50% of the delivered dose, and there is more variability in the high dose regions. On the other hand,

clustering the 10 beams around the “metric” direction removes this overdosing and the results approach the quality of the 18 beam treatment.

3.3 Beam Front Filtering and the Positivity Constraint

A non-intuitive component of tomographic dose inversion in equation (15) is the high-pass filter operator I_0^{-1} in equation (14), which arises mathematically from the Fourier space coordinate transformation in the Projection-Slice Theorem (Natterer 1986). The filter is the source of negative fluence in equation (15) that is removed by the positivity constraint. The impact of the filter can be clearly seen for the Gaussian ellipse dose prescription because of the existence in equation (36) of a single angle-dependent boundary point ξ_0 for negative fluence on the beam defined by the condition

$$E(\xi_0) = \frac{1}{2\xi_0} \exp(\xi_0^2) \quad (43)$$

where

$$\xi_0 = s / \omega(\theta), \quad (44)$$

which is numerically equal to about 10.0. In figure 6 the beam front function, $f(\theta, s)$ in equation (36), is plotted at θ of zero for the Gaussian ellipse in equation (30) before and after the application of the filter. Note that the effect of the filter is to create unphysical negative fluence (hatched region). These outlying regions of the beam front are set to zero by the positivity constraint. The beam front before filtering is completely positive, yet wider than the positive region of the beam front after filtering.

An important question is of the need for the filter in dose reconstruction; that is, whether the filter plus positivity constraint is superior to direct projection to a positive fluence (see also Bortfeld *et al* 1990, Mackie *et al* 1993, Holmes and Mackie 1994). Figure 7 contains the delivered dose reconstruction and scatterplot for the Gaussian ellipse without the filter for 50 evenly spaced beams. Compared to the results seen in figure 5 for 50 beams with the filter, far superior dose conformation is obtained through the use of the filter and positivity constraints. The removal of the filter results in a large tissue overdose and a poor match between the prescribed and delivered dosages.

3.4 Sampling Effects and Beam Front Filtering

In practice, the beam front $f(\theta, s)$ in equation (15) must be sampled in both angle θ and beam front s coordinates. The beam front filters $I_{-\mu}^{-1}$ and κ_{μ}^{-1} effectively boost high spatial frequencies, so it is expected that the Nyquist sampling condition (Oppenheim 1978), $W_{\max} = \frac{2\pi}{\Delta s}$, where Δs is the beam front sampling increment, will impose a sharp frequency cutoff, W_{\max} , on the filtered beam. The other frequency scale in the problem, due to sampling in θ , is the “Bow Tie” condition in equation (22), $W'_{\max} = \frac{2N}{\pi R}$, which depends on the size and spatial frequencies in the *delivered* dose.

In tomographic imaging, an additional weighting function or taper reducing high frequencies is usually applied to the beam front filter to mitigate measurement noise (see figure 8). Tapered filters have also been used in tomographic IMRT (Bortfeld *et al* 1990, Mackie *et al* 1993, Holmes and Mackie 1994, Levine *et al* 1999) and their fall-off has been tied to the “Bow Tie” frequency bound. The taper reduces the effect of filter “ringing” or Gibb’s phenomenon which would occur with a square frequency window. The result is a smoothing of the filtered beam front and reduced inhomogeneities in the delivered dose. However, dose prescriptions typically have high frequency

content, a fixed value on the tumor and zero elsewhere, and their projections may not be band-limited (Bortfeld and Boyer 1995). Consequently, tapering reduces high frequency inhomogeneities on the tumor, but at the expense of a low frequency spread of the dose. The spread causes added exposure to the surrounding tissues and some variation of the dose over the tumor which in a clinical setting is to be avoided. To compensate for this, we have modified the filtering process for “hard-edged” dose prescriptions. The taper is replaced by an averaging over the filtered projection and the addition of a small dc component to the non-zero part of the positively constrained filtered projection. (Gaussian dose prescriptions which are low frequency band-limited functions effectively taper the high frequency filter automatically.) This results in good homogeneity across the tumor and dose edges that are very sharp, while diminishing high frequency filter “ringing”. The introduction of a dc component to the IMRT beam filter has been discussed in Bortfeld and Boyer 1995. We also note that related approaches have used iterative schemes to build in a dose edge (Bortfeld *et al* 1990).

Preferred beam directions, the retention of high frequencies in the projected dose, and the addition of a dc component are better understood when the problem is cast into frequency space sampling using the $\mu \rightarrow 0$ Projection-Slice Theorem in equation (17). Figure 9 contains a sketch of the magnitude of the 2D Fourier transform of the Gaussian ellipse prescribed dose in equations (30) and (31) elongated in the x -direction. From equation (17) the frequency space samples of the beam at angle θ directly sample the θ -slice through the function. Note that the elongation of the tumor in the x -direction corresponds to an elongation of its 2D transform in the frequency space k_y -direction. Consequently, sampling this function in the angle range indicated, with the implicit zeroing of samples outside the cone, is most efficient. The Fourier transform of a similarly oriented “hard edged” dose prescription, defined with constant value within an elliptical shape and zero

elsewhere as discussed in Section 4, would have similar properties. The linear frequency filter, $I_{-\mu}^{-1}$, which was derived assuming continuous sampling in angle, compensates for the over-sampling at low frequencies and the linear decrease in sample density with distance from the origin. However, due to clinical implementation and delivered dose constraints the beam numbers can be very small (5-9), and the sampling density argument for $I_{-\mu}^{-1}$ then breaks down, suggesting either the removal or modification of the filter (Bortfeld and Boyer 1995). The addition of a dc component thus partially compensates for the use of relatively low beam numbers. However, for limited sampling in angle, it would also seem beneficial to retain the largest frequency range possible.

The classical “Bow Tie” condition in equation (22) is an extremely conservative bound for a situation where the reconstructed function is not known *a priori*. In this case, uniform sampling of $\hat{P}(k_x, k_y)$ in angle and frequency over the indicated range is warranted. However, in a situation where the function $\hat{P}(k_x, k_y)$ is known, a (θ, k) representation of \hat{P} in Gabor or wavelet (Gabor 1946, Harpen 1998) functions with the application of a local Nyquist condition should allow for the design of optimum angle sampling and θ -dependent beam front filters.

4. “Hard-edged” Elliptical Dose Functions

At the present time tumor dose prescriptions are typically single- (or at most, double-) valued functions reflecting an estimated threshold for local control. The goal is for dose homogeneity on the tumor with a sharp dose edge at the boundary with normal tissue. In this section the IMRT tomographic formalism developed in Section 2 is applied to this type of dose prescription. In order to judge conformation to a single-valued dose prescription the dose-volume-histogram (DVH) is computed. The cumulative DVH is defined as the percent volume less than a delivered dose value

versus the dose (Drzymala *et al* 1991). Perfect dose conformation corresponds to a step function for the tumor DVH; and the goal of minimum tissue exposure corresponds to the tissue DVH at small values of the dose and exposed volume.

In Section 4.1, simple convex prescribed dose shapes are examined to illustrate “beam selection” based on the beam overlap metric. By selecting beams where the metric is largest, a delivered dose can be achieved which approaches the results for larger numbers of evenly spaced beams. Section 4.2 extends these ideas to more complicated concave prescribed dose shapes which can surround a sensitive organ. For these more complicated shapes, beam selection is less pronounced. However, it is shown that it is crucial to include beam directions where the metric is large, especially for low numbers of beams.

4.1 Convex Dose Functions

Figure 10 shows results for a “hard ellipse” dose prescription defined to be 1.0 inside a set of points (x,y) such that

$$\frac{x^2}{a^2} + \frac{y^2}{b^2} < 1 \quad (45)$$

and zero elsewhere. We consider the case of $a = 4.0cm$ and $b = 0.5cm$. Delivered dose contours are shown for 8, 4 and 2 evenly spaced beams between 0^0 and 180^0 . As seen in the tumor DVH, all beam number results show good homogeneity on the tumor. The surrounding normal tissue (SNT) is defined as the area within $1cm$ of the tumor boundary. At higher doses, the SNT DVH shows that the 8 and 4 beam exposed volumes are nearly zero, and the 2 beam exposure is about 10 % of the volume. This mainly comes from the heavy weighting of the 90^0 beam, and the inability of just two beams to carve out the elliptical shape near the dose edge. Starting at about 60 % of the prescribed

dose, however, the SNT DVH for 2 beams is actually superior. This arises from the limited angle in tissue exposed by the 0^0 and 90^0 beams. Clearly, from the contours and DVHs there is a saturation effect: as the number of beams is increased the contours are more conforming, and more of an elliptical shape is reproduced in the delivered dose. However, there is also a trade-off between high and low dose contributions in the SNT DVH with the number of beams which comes about from the definition of the SNT. Figure 10 shows the beam metric for this prescribed dose which, like the Gaussian or “soft” ellipse, is heavily weighted toward the narrow directions (90^0 and 270^0). The results for 4 beams placed between 70^0 and 110^0 , where the beam metric is largest, is also shown. The SNT DVH for this “metric” beam configuration has almost zero volume for high dose, like the 4 and 8 evenly spaced beams, and is also small for the low dose like the 2 beam result. The clustering near 90^0 for the “metric” beams limits tissue exposure like the 2 beam result, but is also very conforming like the 4 and 8 evenly spaced beam results. Overall, the “metric” beams appear to be in a superior configuration.

The interpretation of tomographic IMRT as a frequency space sampling problem applies as well to “hard” dose prescriptions. The 2D Fourier transform of the hard ellipse dose prescription $\Omega[(x/a)^2 + (y/b)^2 - 1]$ in equation (45) is given by

$$\hat{\Omega}(k_x, k_y) = \frac{2\pi ab J_1(\sqrt{a^2 k_x^2 + b^2 k_y^2})}{\sqrt{a^2 k_x^2 + b^2 k_y^2}}, \quad (46)$$

where J_1 is the first order Bessel function and (k_x, k_y) is the frequency space coordinate (see Gradshetyn and Ryzhik 1965 reference). This function requires more complicated sampling than the Gaussian in equation (31) because 1) the asymptotic fall-off for large arguments (Gradshetyn and Ryzhik 1965) is proportional to the more gradual function $(a^2 k_x^2 + b^2 k_y^2)^{-3/4}$, and 2) the J_1 -function

oscillates. The oscillatory behavior of J_1 suggests the need for higher frequency space sampling, even though the general shape of $\hat{\Omega}(k_x, k_y)$ is the same as in Figure 9.

Figure 11 illustrates the importance of the filter in achieving a conforming dose. Beam fronts, contour plots and DVH's are shown for 50 beam plans (above beam number saturation) with and without beam front filtering for the "hard ellipse". The beam front without filtering is simply the projection of the prescribed dose, and at 0^0 is parabolic with the maximum in the center. The beam front after application of the filter and dose constraint is quite flat, similar to the analytic result for a disk (Bortfeld and Boyer 1995). The beam front filter thus creates a sharp dose edge and uniform dose across the tumor. The importance of including the filter is clear when the delivered dose contour plots, and tumor and SNT DVH's are examined. For this case the SNT region is defined to be $2cm$ around the tumor boundary. Due to large dose inhomogeneity on the tumor for the no-filter case, we have normalized the dose to be greater than or equal to the prescribed dose over 100 % of the tumor volume. The tumor SNT for the no-filter case varies by a factor of two over the tumor, while the filtered results vary by about 20 %. The SNT results are also superior in the filtered case for the entire volume. In general it was found that removing the filter or significantly decreasing the high frequency content of the projected dose also removed the benefits of beam orientation selection.

Figure 12 shows results for a "peanut-shaped" tumor consisting of two overlapping spheres with radii of $1.0cm$, meant as a prototype for cranial tumors treated with two isocenters (Shiu *et al* 1997). As with the hard ellipse, the contour plots appear to achieve a more conforming dose with increasing beam numbers. The 24 beam delivered dose approaches the beam number saturation point for reconstruction of the prescribed dose as judged by the dose contours, although the 8 beam result is nearly as good as judged by the DVHs. Homogeneity over the tumor volume for all dose

prescriptions is very good. As in the ellipse case, the 24 and 8 beam SNT DVH's show slightly less exposure for high dose compared to the 4 beam result. Although the beam overlaps (not shown) were most heavily weighted at the 90^0 and 270^0 directions, as with the ellipse, the magnitudes were not much greater than the other directions. Accordingly, very weak beam orientation selectivity was found, and it was not clear if these delivered doses were superior to the equally spaced beams from 0^0 to 180^0 .

Figure 13 shows results for a hard ellipse with a nearby spherical organ-at-risk. The tumor ellipse has $a = 2.4cm$ and $b = 1.2cm$. The organ-at-risk has a radius of $1.0cm$ and is separated by $0.5cm$ of normal tissue from the tumor. To reduce dose to the organ-at-risk, an unphysical prescription of -1.0 was assigned to it. Results are shown for 24, 8, and 4 evenly spaced beams and 4 selected beams between 60^0 and 120^0 . As with the other shapes for evenly spaced beams, the results improve with larger beam numbers, and reach a saturation level somewhere between 8 and 24 beams, with the exception that the 4 evenly spaced beams have less organ-at-risk dose at very low doses. Like the ellipse discussed above, the beam selection metric is most heavily weighted in the 90^0 direction. The presence of the organ-at-risk in this case reduces the importance of the 0^0 direction compared to the tumor alone. A "selected" four beam plan between 60^0 and 120^0 has a dose variation of less than 10% over the tumor and markedly less organ-at-risk dose than any of the other plans. In this case the directions which contribute most to a conforming dose minimize exposure to the organ-at-risk, effectively decreasing from 24 to 4 the number of beams required to achieve a conforming dose.

4.2 Concave Dose Functions

Figure 14a shows a "butterfly" shaped prescribed dose, consisting of two overlapping ellipses. This case is similar to a case examined by Bortfeld and Schlegel 1993 and many other investigators.

In their study Bortfeld and Schlegel 1993 found through a simulated annealing search over angles that for three beams the optimal beam directions were roughly along the long axes of the two ellipses and along one of the diagonals to these axes. We note that these directions along the long axes are the preferred directions seen in the convex single ellipse case examined above. In the figure this would correspond to directions 0° (north-south) and 90° (east-west) for the long axes along the ellipses, and 135° (northeast-southwest) for the diagonal. A plot of the metric overlap function for this prescribed dose in figure 14e shows that this function is largest along these same directions, although in general for concave shapes the metric functions are much less dependent on angle than for the simpler convex prescribed doses examined above. Figure 14b shows a colorwash of the delivered dose for three “metric” beams oriented along these directions. To show the importance of beam placement figure 14c shows the delivered dose for the same directions as figure 14b, except that the most important beam (the 135° beam along the diagonal) has been moved to be along the opposite diagonal (northwest-southeast) at 45° which is a *minimum* of the dose metric function. The resulting delivered dose is less conforming with much more dose to the surrounding normal tissue. To underscore this point, figure 14d shows the delivered dose for three beams clustered near the minimum of the overlap metric at angles 20° , 45° , and 70° . The delivered dose appears much poorer in this colorwash plot. These differences are quantified in figures 14f and 14g which show the tumor and surrounding-normal-tissue (SNT) DVH’s, respectively, for the beam arrangements in figures 14a-c. The SNT extends about 1.5 times beyond the size of the tumor prescribed dose. The tumor DVH’s are all similar. For the beams clustered near the overlap minimum (figure 14d), there is high dose over a substantial part of the SNT. This improves with the better beam placement of figure 14c, and is the best with the optimal beam placement of figure 14b, where the beam overlap metric is largest, although for low doses the results of figure 14d are actually better due to the more limited

angle space of this plan. We find that for larger numbers of beams, the delivered dose is much less sensitive to beam positions, and this agrees with the results of Bortfeld and Schlegel 1993.

Figure 15a shows the prescribed dose function for a “horseshoe” shaped tumor surrounding an organ-at-risk. The prescribed dose for the tumor is set to 1.0. To reduce dose to the organ-at-risk an unphysical dose prescription of -0.1 was assigned to it. Like the “butterfly” tumor examined above, we have found that above a certain number of beams, beam placement is not significant, as long as they evenly cover the angle space. Figure 15b shows the delivered for 12 evenly spaced beams from 0^0 to 180^0 which results in a good conforming dose. However, for lower numbers of beams it is important to explicitly include the directions where the beam metric overlap function is large. Figure 15e shows the beam overlap function for this prescribed dose which has maxima along the 0^0 (north-south) and 90^0 (east-west) directions. These are along the long-axes of the component ellipses which make up the prescribed dose function. Figure 15c shows the delivered dose for 6 “metric” beams evenly spaced so that the metric angles 0^0 and 90^0 are included ($0^0, 30^0, 60^0, 90^0, 120^0, 150^0$). In contrast figure 15d shows the delivered dose for 6 beams evenly spaced but not including the metric angles ($15^0, 45^0, 75^0, 105^0, 135^0, 165^0$). This delivered dose appears less conforming than the 6 “metric” based plan of figure 15c. These differences are evident in the DVH’s shown in figures 15f-h. The tumor DVH for the 12 beam plan is the most uniform and the 6 beam plan shifted from the “metric” directions, figure 15d, is the least. The organ-at-risk DVH’s are all similar. For the SNT DVH the 6 metric beam delivered dose is actually slightly better than the twelve beam plan, but this is probably due to including a very limited part of the tissue space in the SNT.

5. Conclusions

We have reviewed and extended the theory of tomographic dose reconstruction. We derive the basis for a saturation with beam number of dose conformation, and provide an analysis which ranks particular beam orientations in terms of the contribution to the delivered dose. Preferred beam directions are found which effectively reduce the number of beams necessary to achieve a given level of dose conformation. This is done by formally connecting the problem to the tomographic Fourier space sampling of the prescribed dose function. The analysis is a new and unique application of the tomographic Projection-Slice Theorem to the problem of beam orientation determination. Results are applied to simple geometric shape dose prescriptions in two dimensions: a Gaussian ellipse where analytical results can be obtained and a series of hard-edged convex shapes to illustrate beam selection based on the beam overlap metric. More complex concave prescribed dose shapes which contain a sensitive organ are also analyzed, and for low beam numbers are found to have preferred beam directions. The effects of the beam front filter and the positivity constraint are also analyzed. While this constraint results in unavoidable normal tissue exposure, these effects are small and the tomographic approach is superior to dose projection alone.

The modulation of a two-dimensional beamfront, the development of high resolution collimators for intensity modulated radiosurgery (Cardinale *et al.* 1998), and non-coplanar radiotherapy all suggest the need to examine 3D IMRT. Even for treatments with a cylindrical axis of symmetry, it is likely that the optimum 2D beam locations will vary between slices. A fully three-dimensional analysis of projection IMRT, involving the 3D Fourier transform of the prescribed dose function and spherical harmonic expansions with a generalized Projection-Slice Theorem, has appeared in Levine *et al.* 1999. The examples studied suggest that higher levels of dose conformation are possible, beam

selection is important, and beam numbers are comparable to 2D treatments. A systematic examination of preferred directions and sufficient beam numbers for 3D dose prescriptions using the tomographic approach is the focus of our current research. These results could provide a robust starting point for more refined global search methods for optimum beam numbers and directions in three dimensions.

While this manuscript was being prepared Oelfke and Bortfeld 1999 discovered alternative solutions to the tomographic IMRT problem. For $\mu=0$ the solutions of Eq. (15) are symmetric for opposing beams; a condition that can be lifted for possible enhanced dose conformation. An examination of beam orientation selection involving this more general class of solutions is an interesting area of future research.

Acknowledgments:

We would like to thank Dr. Y.C. Lo for suggesting the use of the surrounding normal tissue (SNT) DVH as a measure of dose conformation. Drs. M.M. Urie and Y.C. Lo are also thanked for discussions on clinical applications of IMRT tomographic inversion. This work was supported by the NIH small business innovative research (SBIR) program, grant number 1R43CA82027-01.

References

1. Boyer A L 1994 Radiation Therapy Beam Modulation Techniques *Syllabus: A Categorical Course in Physics: Three-dimensional Radiation Therapy Treatment Planning* eds J A Purdy and B A Fraas (Oak Brook, IL: RSNA Publications)
2. Bortfeld T and Boyer A L 1995 The Exponential Radon Transform and Projection Filtering in Radiotherapy Planning *Int. J. Imaging Systems and Technology* **6** 62-70
3. Bortfeld T, Burkelbach J, Boesecke R, and Schlegel W 1990 Methods of image reconstruction from projections applied to conformal radiotherapy *Phys. Med. Biol.* **35** 1423-1434
4. Bortfeld T and Schlegel W. 1993 Optimization of beam orientations in radiotherapy: some theoretical considerations *Phys. Med. Biol.* **38** 291-304
5. Bortfeld T, Kahler D, Waldron T, and Boyer A 1994 X-ray Field Compensation with Multileaf Collimators *Int. J. Radiation Oncology Biol. Phys.* **23** 723-730
6. Bortfeld T, et.al. 1994 Realization and verification of three-dimensional conformal radiotherapy with modulated fields *Int. J. Radiat. Oncol. Biol. Phys.* **30** 899-908
7. Brahme A, Roos J E, and Lax I 1982 Solution of an integral equation encountered in rotation therapy *Phys. Med. Biol.* **27** 1221-1229
8. Cardinale R M, Benedict S H, Wu Q, Zwicker R D, Gaballa H E, and Mohan R 1998 A Comparison of three Stereotactic Radiotherapy Techniques; Arcs vs. Noncoplanar Fixed Fields vs. Intensity Modulation *Int. J. Radiation Oncology Biol. Phys.* **42** 431-436
9. Censor Y, Altschuler M D, and Powlis W D 1988 A Computational Solution of the Inverse Problem in Radiation-Therapy Treatment Planning *Applied Mathematics and Computation* **25** 57-87

10. Cho P, Lee S, Marks R J, Oh S, Sutlief S G, and Phillips M H 1998 Optimization of intensity modulated beams with volume constraints using two methods: Cost function minimization and projections onto convex sets *Med. Phys.* **25** 435-443
11. Cormack A M 1987 A Problem of Rotation Therapy with X-rays *Int. J. Radiat. Oncol. Biol. Phys.* **13** 623-630
12. Cormack R A 1998 Beam Profiles for X-ray Rotation Therapy *Med. Phys.* **25** 879-884
13. Cormack A M and Cormack R A 1987 A Problem in Rotation Therapy II: Dose Distributions with an Axis of Symmetry *Int. J. Radiat. Oncol. Biol. Phys.* **13** 1921-1925
14. Cormack A M and Quinto E T 1989 On a Problem in Radiotherapy: Questions of Non-negativity *Int. J. Imaging Syst. Technol.* **1** 120-124
15. Cormack A M and Quinto E T 1990 The Mathematics and Physics of Radiation Dose Planning using X-rays *Contemporary Mathematics* **113** 41-55
16. Crowther R A, DeRosier D J, and Klug A 1970 The reconstruction of a three-dimensional structure from projections and its application to electron microscopy *Proc. Roy. Soc. Lond. A.* **317** 319-340
17. Drzymala R E, Mohan R, Brewster L, Chu J, Goitein M, Harms W, and Urie M M 1991 Dose-Volume Histograms *Int. J. Radiat. Oncology Biol. Phys.* **21** 71-78
18. Gabor D 1946 The Theory of Communication *J. Inst. Elec. Eng.* **93** 429-457
19. This follows from the generating integral for Bessel functions and the differential equation relating the order zero and one Bessel function, $(zJ_1)' = zJ_0$, found in Gradshetyn I S and Ryzhik I M 1965 *Tables of Integrals, Series and Products* (New York, NY: Academic Press).
20. Gregerson E A, Levine R Y, and Urie M M 1995 Beam Sampling and Selection for 3D Conformal Radiotherapy (abstract) *Med. Phys.* **22** 920

21. Haas O C L, Burnham K J, and Mills J A 1998 Optimization of beam orientation in radiotherapy using planar geometry *Phys. Med. Biol.* **43** 2179-2193
22. Harpen M D 1998 A Introduction to Wavelet Theory and Application for the Radiological Physicist *Med. Phys.* **25** 1985-1993
23. Holmes T and Mackie T R 1994 A filtered backprojection dose calculation method for inverse treatment planning *Med. Phys.* **21** 303-313
24. Johns H E and Cunningham J R 1983 *The Physics of Radiology, Fourth Edition* (Springfield, Il:Thomas)
25. Lee S, Cho P S, Marks R J, and Oh S 1997 Conformal radiotherapy computation by the method of alternating projection onto convex sets *Phys. Med. Biol.* **42** 1065-1086
26. Levine R Y, Gregerson E A, and Urie M M 1999 The application of the x-ray transform to 3D conformal radiotherapy *Computational Radiology and Imaging: Therapy and Diagnostics* ed C Borgers and F Natterer (New York NY: Springer-Verlag)
27. Lindgren A G and Rattey P A 1981 The Inverse Discrete Radon Transform with Applications to Tomographic Imaging Using Projection Data *Advances in Electronics and Electron Physics*, **56** 359-410
28. Llacer J 1997 Inverse radiation treatment planning using the Dynamically Penalized Likelihood method *Med. Phys.* **24** 1751-1764 (1997)
29. Mageras G S and Mohan R 1993 Application of fast simulated annealing to optimization of conformal radiation treatments *Med. Phys.* **20** 639-647
30. Mackie T R, Holmes T, Swerdloff S, Reckwerdt P, Deasy J, Yang J, Paliwal B, and Kinsella T 1993 Tomotherapy: A new concept for the delivery of dynamic conformal radiotherapy *Med. Phys.* **20** 1709-1719

31. Medoff B P 1987 Image Reconstruction from Limited Data: Theory and Applications in Computerized Tomography *Image Recovery: Theory and Application* ed H Stark (New York, NY: Academic Press)
32. Natterer F 1986 *The Mathematics of Computerized Tomography* (New York, NY:J Wiley and Son)
33. Niemierko A 1992 Random search algorithm (RONSC) for optimization of radiation therapy with both physical and biological end points and constraints *Int. J. Radiation Oncology Biol. Phys.* **23** 89-98
34. Oelfke U and Bortfeld T 1999 Inverse planning for x-ray rotation therapy: a general solution of the inverse problem *Phys. Med. Biol.* **44** 1089-1104
35. Oldham M, Khoo V S, Rowbottom C G, Bedford J L, and Webb S 1998 A case study comparing the relative benefit of optimizing beam weights, wedge angles, beam orientations and tomotherapy in stereotactic radiotherapy of the brain *Phys. Med. Biol.* **43** 2123-2146
36. Oppenheim A V 1978 *Applications of Digital Signal Processing* (Englewood Cliffs, N.J.: Prentice Hall)
37. Rosen I I, Lane R G, Morill S M, and Belli J A 1991 Treatment plan optimization using linear programming *Med. Phys.* **18** 141-152
38. Rowbottom C G, Webb S, and Oldham M 1998 Improvements in prostate radiotherapy from the customization of beam directions *Med. Phys.* **25** 1171-1179
39. Shiu A S, Kooy H M, Ewton J R, Tung S S, Wong J, Antes K, and Maor M H 1997 Comparison of Miniature Multileaf Collimator (MMLC) with Circular Collimation for Stereotactic Treatment *Int. J. Radiation Oncology Biol. Phys.* **37** 679-688

40. Soderstrom S and Brahme A 1993 Optimization of dose delivery in a few field techniques using radiobiological objective functions *Med. Phys.* **20** 1201-1210
41. Spirou S V and Chui C-S 1998 A gradient inverse planning algorithm with dose-volume constraints *Med. Phys.* **25** 321-332
42. Stein J, Mohan R, Wang X-H, Bortfeld T, Wu Q, Preiser K, Ling C C, Schlegel W 1997 Number and orientations of beams in intensity-modulated radiation treatments *Med. Phys.* **24** 149-160
43. Webb S 1989 Optimisation of conformal radiotherapy dose distributions by simulated annealing *Phys. Med. Biol.* **34** 1349-1370
44. S. Webb 1991 Optimisation of conformal radiotherapy dose distributions by simulated annealing:
2. Inclusion of scatter in the 2D technique *Phys. Med. Biol.* **36** 1227-1237
45. Webb S 1993 *The Physics of Three-dimensional Radiation Therapy, Conformal Radiation Therapy, Radiosurgery, and Treatment Planning* (Philadelphia: IOP Publishing)

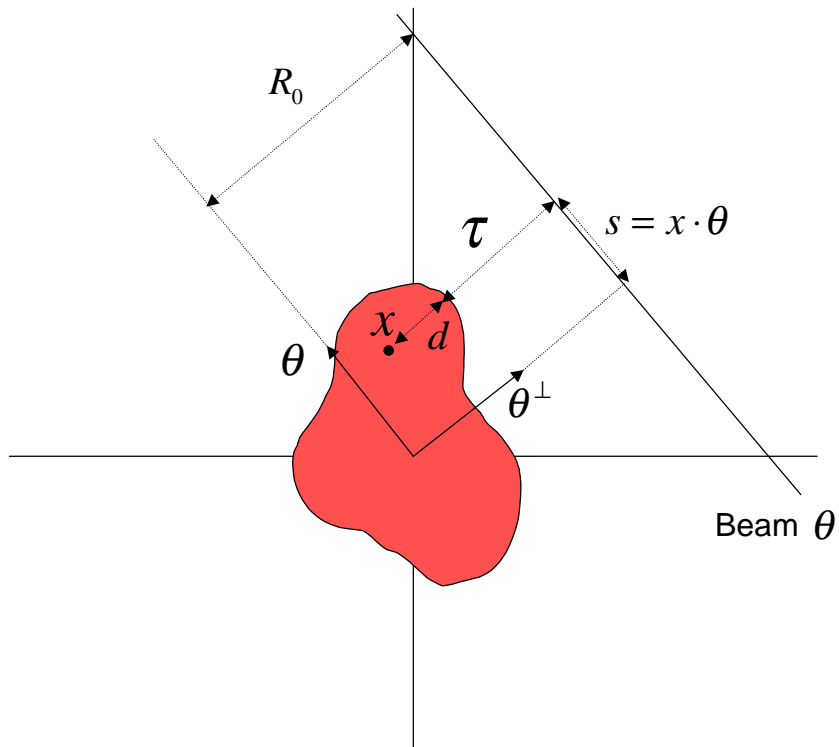


Figure 1. Geometry of 2D IMRT Tomographic Inversion.

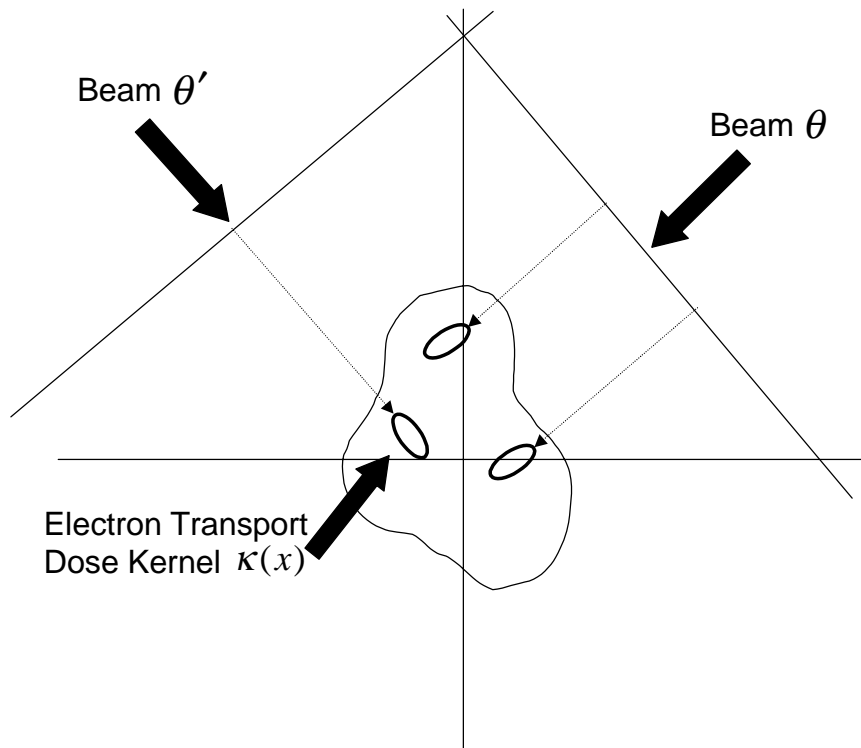


Figure 2. Dose Deposition Model for 2D Tomographic IMRT. The small ellipses within the tumor are dose kernels, $\kappa(x)$, centered on a dose deposition point for the rays depicted as arrows for beam directions θ and θ' .

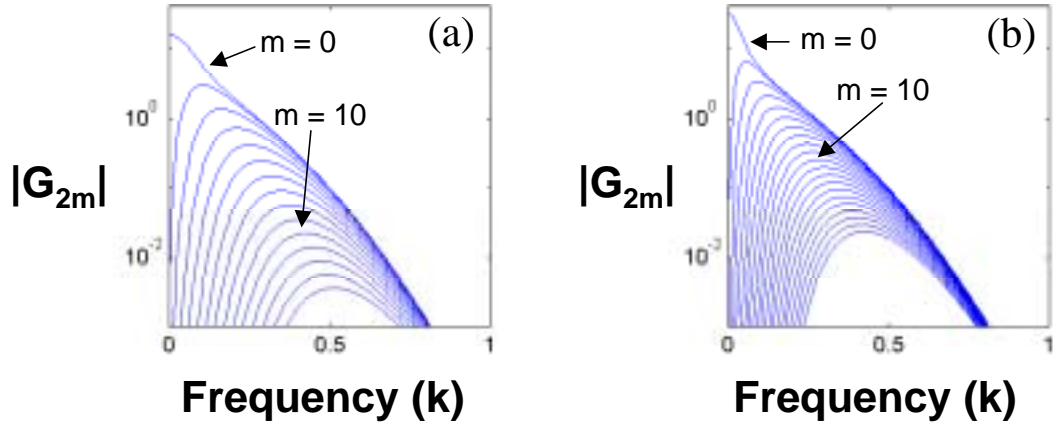


Figure 3. Absolute value of Gaussian ellipse cylindrical harmonics versus frequency. (a) for the case $(a,b)=(5,1)$. (b) for the case $(a,b)=(10,1)$.

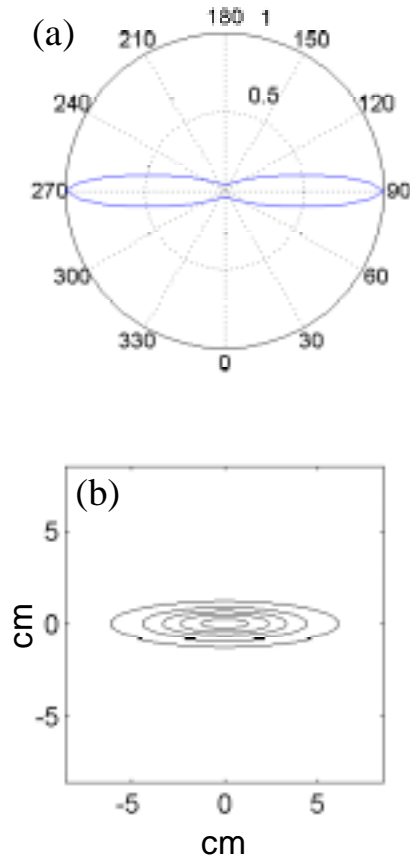


Figure 4. (a) Polar plot of beam selection metric for Gaussian ellipse with $a=4.0\text{cm}$ and $b=0.8\text{cm}$. The metric has been normalized to maximum of 1.0. The zero degree direction corresponds to fluence traveling from the bottom to the top of the figure. (b) Contour plot of prescribed dose for the $a=4.0\text{cm}$ and $b=0.8\text{cm}$ Gaussian ellipse. Contours are at .1,.3,.5,.7 and .9.

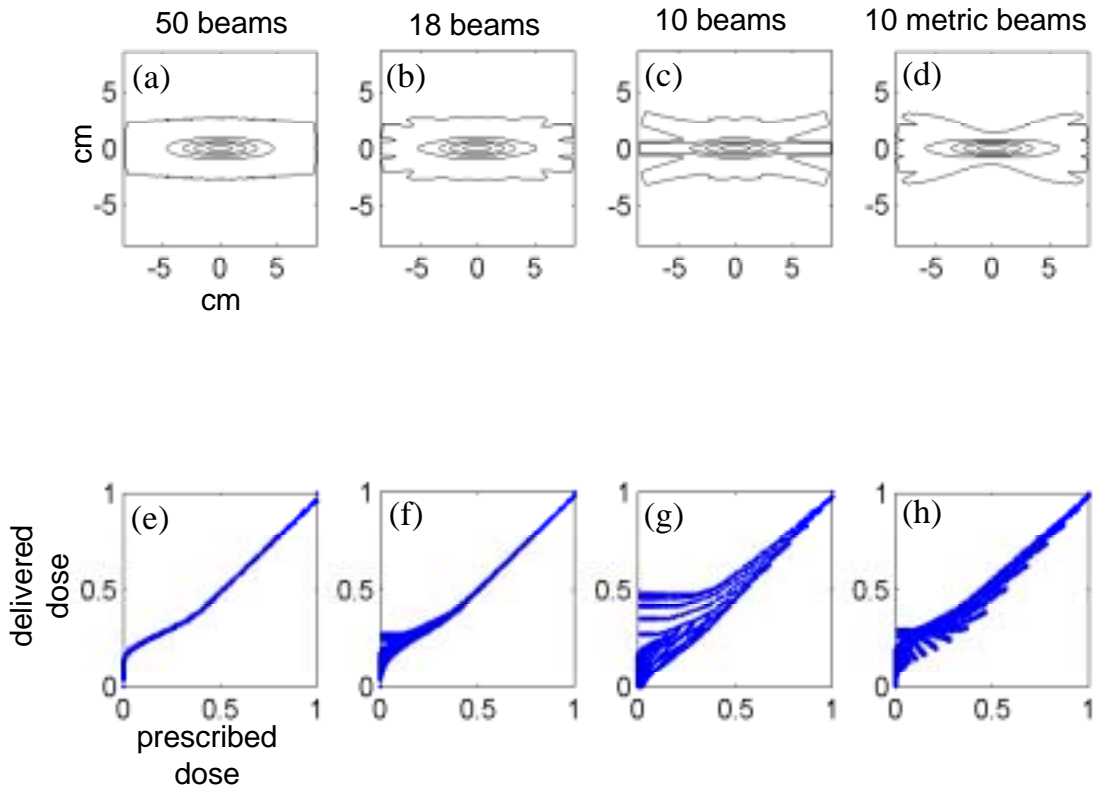


Figure 5. (a-d) Isodose contours for Gaussian ellipse described in figures 4a-c. Contours for 50, 18, and 10 beams equally spaced in angle from 0° to 180° . (d). Contours for 10 evenly spaced beams in the range $45^\circ - 135^\circ$. (e-h) Scatterplots of prescribed versus delivered dose for the contours in (a-d), respectively. Contours are at 0.1, 0.3, 0.5, 0.7 and 0.9.

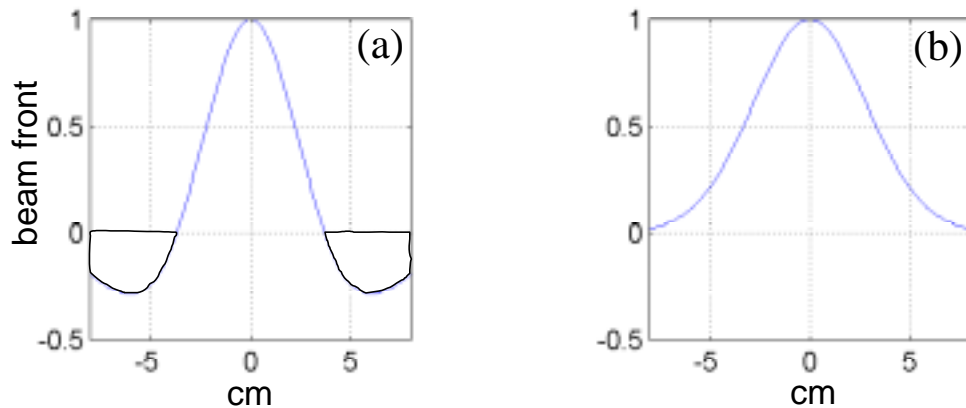


Figure 6. Modulated 0° beam fronts for the Gaussian ellipse with $a=4.0\text{cm}$ and $b=0.8\text{cm}$ (a) with beam front filtering and (b) without beam front filtering. Shaded areas are values of the beam front removed by the positivity constraint. Beams are normalized to maximum of 1.0.

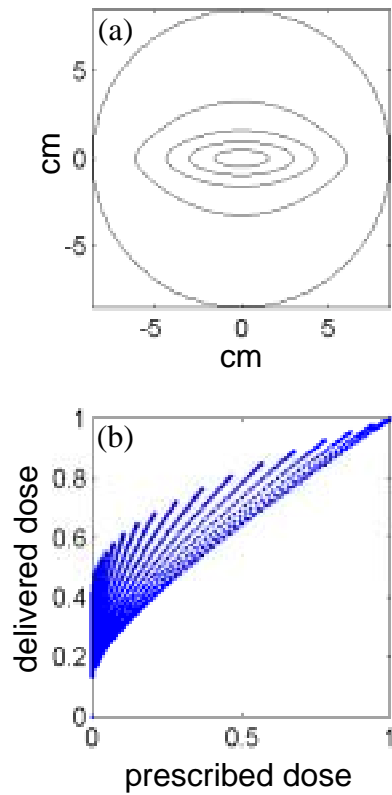


Figure 7. (a) Isodose contours of the delivered dose for the Gaussian ellipse without beam front filtering for 50 equally spaced beams. Contours at .1, .3, .5, .7, and .9. (b) Prescribed versus delivered dose for the Gaussian ellipse without beam front filtering for 50 equally spaced beams.

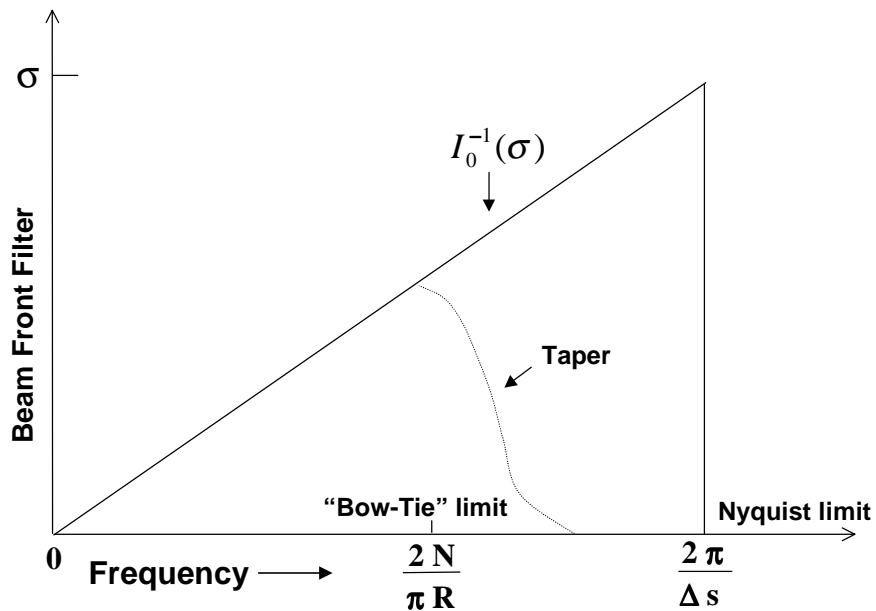


Figure 8. Beam front filter versus frequency.

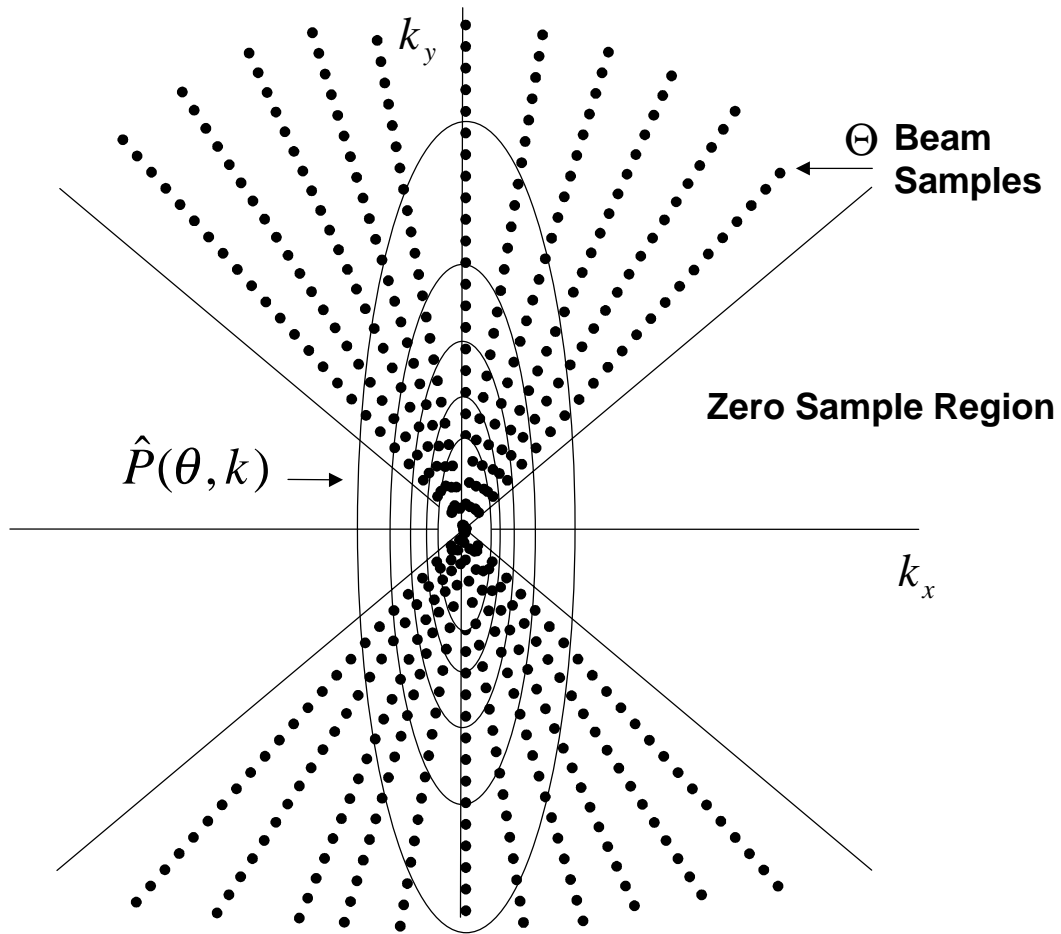


Figure 9. Sketch of 2D Fourier transform and beam sampling of elliptical prescribed dose function. Beam fronts along the “metric” East-West directions correspond to sampling along the k_y axis.

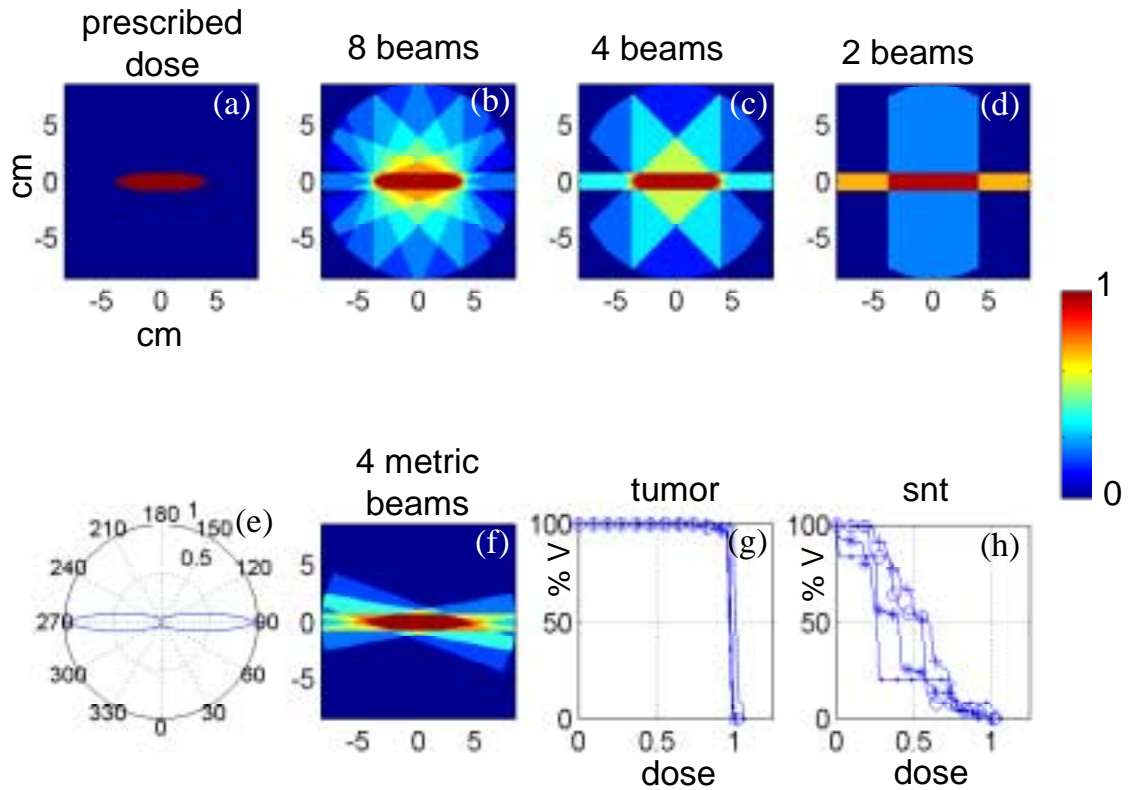


Figure 10. (a-d) Prescribed and delivered dose colorwash images for a “hard ellipse with $a=4.0\text{cm}$ and $b=0.5\text{cm}$ with 8, 4, and 2 equally spaced beams in angle range 0° to 180° . (e) Beam selection metric for “hard” ellipse normalized to maximum of 1.0. Zero degrees from the bottom of the page. (f) Delivered dose using 4 beams selected between 70° and 110° . (g-h) Dose-Volume Histograms (DVH) for tumor and Surrounding Normal Tissue (SNT) for 8 beams (+), 4 beams (o), 2 beams (.), 4 metric beams (*).

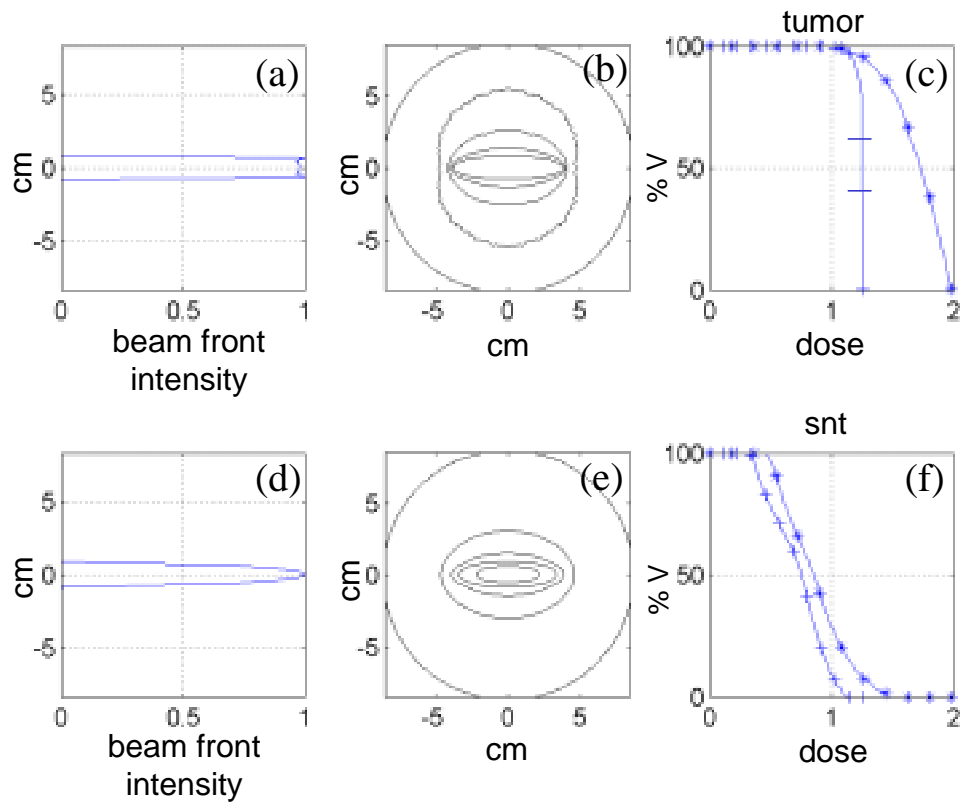


Figure 11. (a-b) Results for “hard” ellipse with beam filtering for 50 evenly spaced beams between 0° and 180° . (a) Beam front at 0° ; (b) isodose contours at 0.1, 0.3, 0.5, 0.7, and 0.9; (d-e) Same as (a-b) without beam front filtering. (c) tumor DVH for 50 even beams with filtering (+) and without filtering (*); (f) same as (c) for SNT DVH.

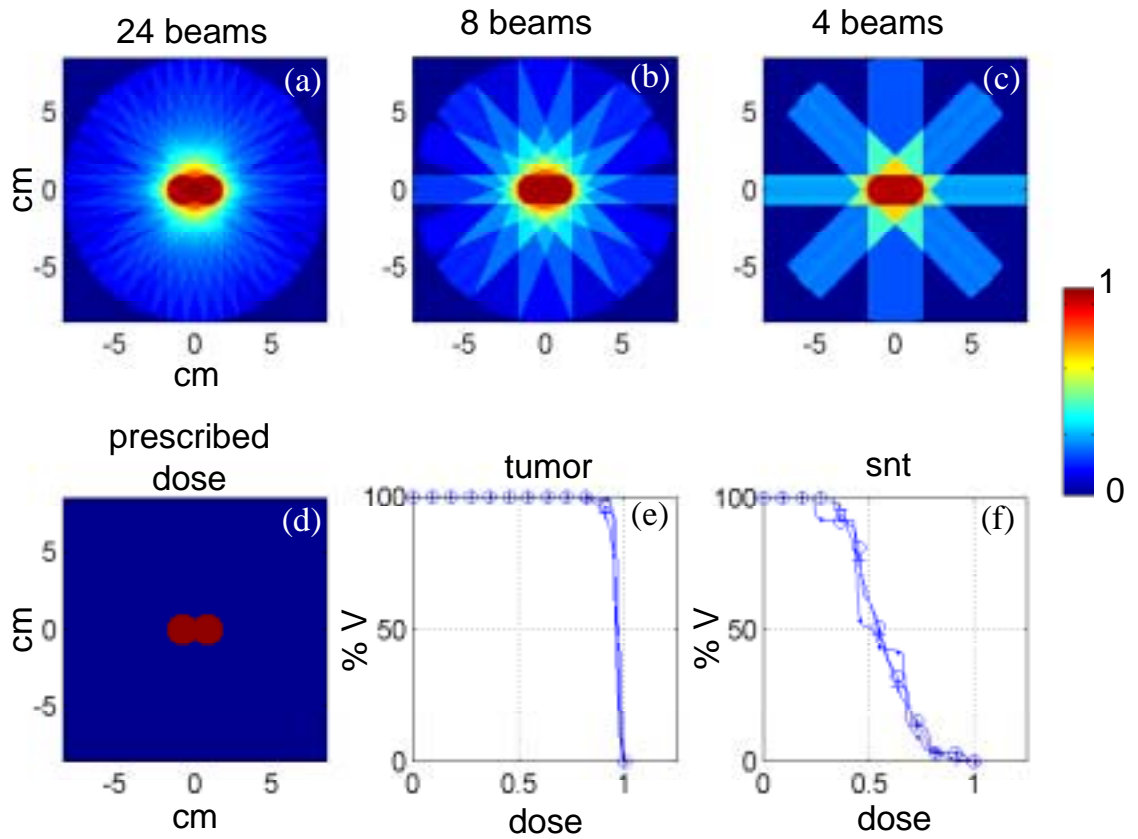


Figure 12. Results for “peanut” shaped tumor consisting of two overlapping spheres with radii of 1.0 cm . (a-c) Colorwash images for 24, 8, and 4 beams evenly spaced between 0° and 180° . (d) prescribed dose for “peanut” shaped tumor; (e) tumor DVH for 24 even beams (+), 8 even beams (o), 4 even beams (.); (f) same as (e) for surrounding normal tissue.

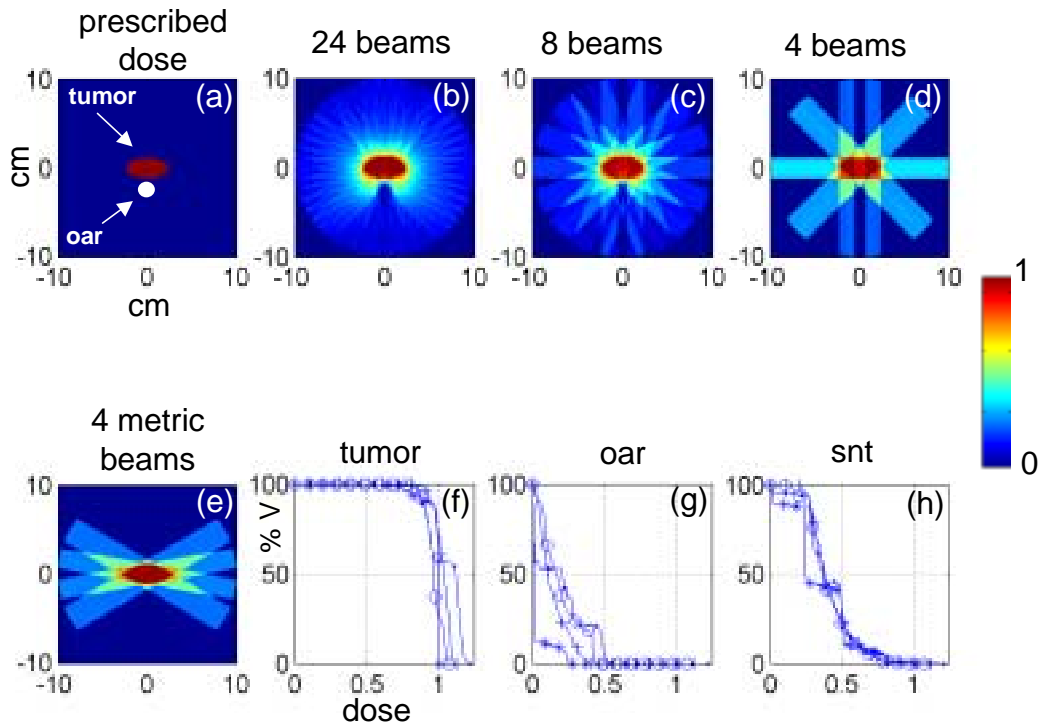


Figure 13. Results for hard ellipse tumor with spherical organ-at-risk; (a) prescribed dose function where tumor ellipse has $a = 2.4\text{cm}$ and $b = 1.2\text{cm}$. The organ-at-risk has a radius of 1.0cm and has 0.5cm of normal tissue between it and the tumor. (b-d) Colorwash images for 24, 8, and 4 beams evenly spaced between 0° and 180° respectively; (e) Delivered dose for 4 beams selected between 60° and 120° (f) tumor DVH for 24 even beams (+), 8 even beams (o), 4 even beams (.), and 4 selected beams (*); (g) same as (f) for organ-at-risk; (h) same as (f) for surrounding normal tissue.

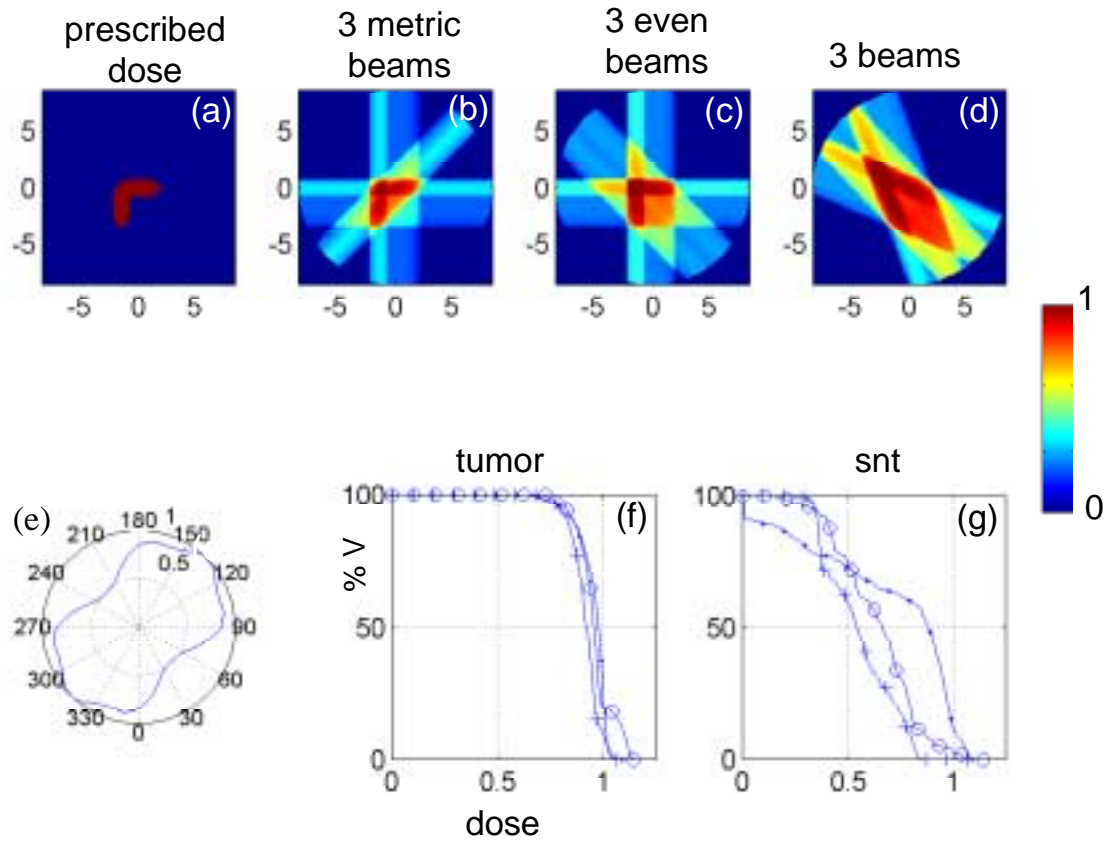


Figure 14. Results for “butterfly” shaped tumor consisting of two overlapping ellipses; (a) prescribed dose function. (b-d) Delivered dose colorwash images for three beams at $(0^\circ, 90^\circ, 135^\circ)$, $(0^\circ, 45^\circ, 90^\circ)$, and $(20^\circ, 45^\circ, 70^\circ)$, respectively. (e) Beam selection metric for prescribed dose normalized to maximum of 1.0. Zero degrees points to the bottom of the page. (f) tumor DVH for three beams at $(0^\circ, 90^\circ, 135^\circ)$ (+), three beams at $(20^\circ, 45^\circ, 70^\circ)$ (o), and three beams at $(20^\circ, 45^\circ, 70^\circ)$ (.), (g) same as (f) except for surrounding normal tissue.

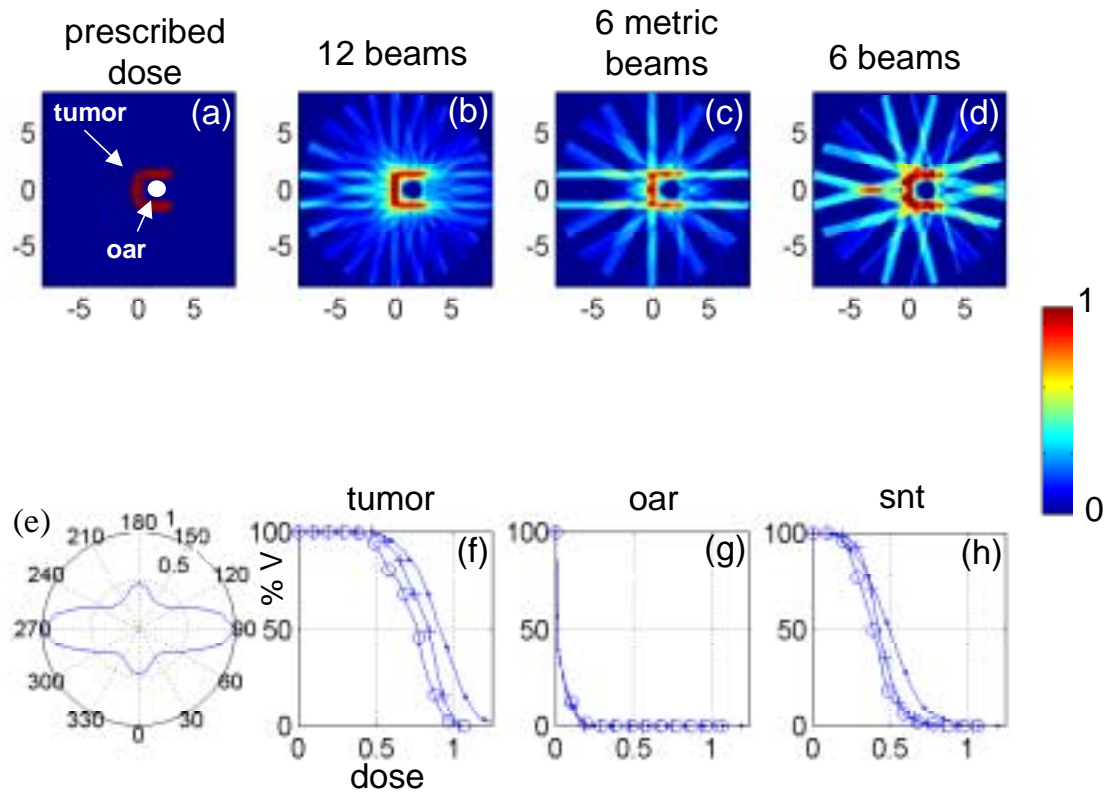


Figure 15. Results for “horseshoe” shaped tumor surrounding an organ-at-risk; (a) prescribed dose function. (b-d) Delivered dose colorwash images for 12 evenly spaced beams, 6 “metric” beams, and 6 beams displaced away from the metric angles; respectively. (e) Beam selection metric for prescribed dose normalized to maximum of 1.0. Zero degrees points to the bottom of the page. (f) tumor DVH for 12 evenly spaced beams (+), 6 “metric” beams (o), and 6 beams displaced away from the metric angles (.); (g) same as (f) except for organ-at-risk. (h) same as (f) except for surrounding normal tissue.